Magnetic structure investigation of the intercalated transition metal dichalcogenide $V_{1/3}NbS_2$

A. E. Hall,[1,*] D. D. Khalyavin,[2] P. Manuel,[2] D. A. Mayoh,[1] F. Orlandi,[2]
O. A. Petrenko,[1] M. R. Lees,[1] and G. Balakrishnan[1,†]
[1]*Department of Physics, The University of Warwick, Coventry CV4 7AL, United Kingdom*
[2]*ISIS Facility, Rutherford Appleton Laboratory, Harwell, Oxford, Didcot OX11 0QX, United Kingdom*

(Received 24 February 2021; revised 14 April 2021; accepted 3 May 2021; published 25 May 2021)

We investigate the temperature evolution of the magnetic structure of $V_{1/3}NbS_2$ using neutron diffraction techniques. We find that $V_{1/3}NbS_2$ has two propagation vectors: $\mathbf{k_0} = (0, 0, 0)$ and $\mathbf{k_1} = (0, 0, \frac{1}{3})$. The $\mathbf{k_0}$ vector can be associated with an antiferromagnetic ordering of in-plane moments with a refined value of $0.90(5)\mu_B$, and $\mathbf{k_1}$ can be associated with moments along the c axis in an up-down-down configuration with refined values of $1.21(12)\mu_B$ and $0.61(6)\mu_B$. Both $\mathbf{k_0}$ and $\mathbf{k_1}$ magnetic components couple with an out-of-plane ferromagnetic moment consistent with magnetization data. Furthermore, single-crystal neutron diffraction shows evidence of diffuse magnetic scattering between the (010) and $(01\pm\frac{1}{3})$ Bragg peaks. We also characterize the field and temperature evolution of the magnetic structure in $V_{1/3}NbS_2$ by magnetic susceptibility and heat capacity measurements. The dc susceptibility measurements give an antiferromagnetic transition temperature of $T_N = 50$ K, and the field scans reveal that the moment does not saturate at magnetic fields up to 100 kOe.

DOI: 10.1103/PhysRevB.103.174431

I. INTRODUCTION

The transition metal dichalcogenides (TMDCs) are a family of materials that have attracted considerable interest over the years due to the properties they exhibit such as superconductivity [1–3], charge density waves [4,5], and even defect-induced magnetism in Mo-based TMDCs [6,7]. The subset of this family that adopts the hexagonal $2H$-XS_2 polytype, where X is a transition metal, crystallizes in structures formed of layers bound together by the weak van der Waals force, allowing thin layers (monolayers, bilayers, etc.) to be isolated via mechanical exfoliation [8]. These layers have been found to exhibit different, and sometimes more exotic, properties that differ from those of the bulk crystal behavior and have been used to successfully synthesize different heterostructures [9].

In this family of materials, magnetic atoms can be intercalated between the layers, and at the critical concentration of $M_{1/3}XS_2$, where M is a $3d$ transition metal, the compounds transform from the hexagonal centrosymmetric space group $P6_3/mmc$ to the hexagonal noncentrosymmetric chiral space group $P6_322$. The intercalated atoms occupy octahedral 2c or 2d Wyckoff positions [10] and form a superlattice of a kind determined by the stoichiometry of the material, with the $M_{1/3}XS_2$ family hosting a $\sqrt{3} \times \sqrt{3}$ structure. These materials can display behavior radically different from the pristine TMDCs. The crystal structure showing the arrangement of the V intercalated in NbS_2, typical of most members of this family of TMDCs, is shown in Fig. 1.

In the $2H$ polytype, the magnetic exchange interactions between the intercalant atoms could be due to the superexchange interactions across the S atoms, the antisymmetric Dzyaloshinskii-Moriya interaction (DMI) due to the noncentrosymmetric structure of the material, or the Ruderman-Kittel-Kasuya-Yosida mechanism through the conduction electrons. The differing strengths of these interactions give rise to the observation of a variety of magnetic phases in the family. This can vary from antiferromagnetism to chiral helimagnetism depending on the nature of the transition metals present in the material [11–13].

Of particular interest are the $Cr_{1/3}NbS_2$ and $Mn_{1/3}NbS_2$ noncentrosymmetric compounds, which have been reported to display chiral helimagnetic behavior [14,15]. Chiral helimagnetism arises in these materials from the competition between the symmetric ferromagnetic exchange interactions and the DMI. The magnetic spins can then form a spiral, conical, or helical structure [16] in response to this competition. Chiral magnets host a wide variety of exotic phenomena, including, but not limited to, the robust, topologically stable chiral soliton lattice (CSL) and the vortex-like magnetic skyrmions [17]. Of the intercalated TMDCs, to date only $Cr_{1/3}NbS_2$ has been proven to host a CSL [18,19]. It has been suggested that this CSL, rather than skyrmions, is formed due to a combination of chiral helimagnetism and strong magnetic anisotropy. Another member of this family, $Fe_{1/3}NbS_2$, exhibits antiferromagnetic behavior at temperatures below 42 K [20,21], with the intercalated Fe atoms forming a triangular lattice. Furthermore, optical measurements of $Fe_{1/3}NbS_2$ suggest that an in-plane nematic director exists in addition to the out-of-plane magnetization [22]. The wide variation in the behaviors of the intercalated TMDCs, depending on the intercalate, has led to great interest in this family.

While many members of this family have been well investigated, there remain several of the intercalated TMDCs that merit further study. One such example is $V_{1/3}NbS_2$, a material that was originally reported as a paramagnet [23] but

*Amelia.Hall@warwick.ac.uk
†G.Balakrishnan@warwick.ac.uk

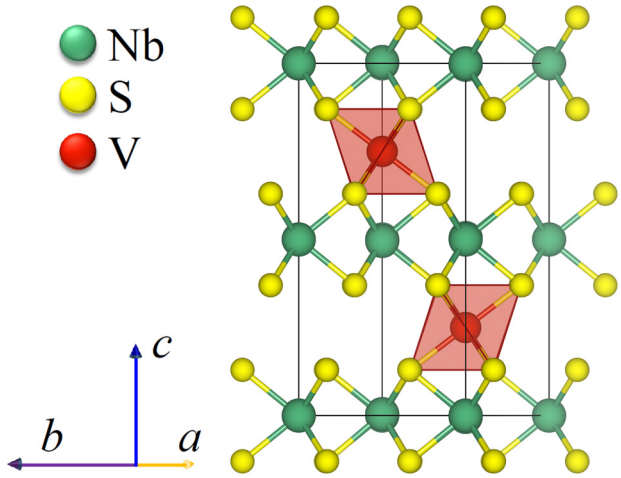

FIG. 1. Structure of $V_{1/3}NbS_2$, which crystallizes in the hexagonal, chiral, noncentrosymmetric $P6_322$ space group, with lattice parameters $a = 5.75$ Å, $c = 12.17$ Å, viewed along the a^* direction. The intercalate, V, is shown in dark red between layers of S and Nb. The octahedra around the V atoms are shown.

was later reported to order ferromagnetically at temperatures below 50 K [11], with an additional transition observed as the temperature decreased below 20 K and the field was directed perpendicular to the c axis. It has since been predicted that $V_{1/3}NbS_2$ could host a chiral soliton lattice using calculations that consider the effect of spin-orbit coupling [24].

Interestingly, the paramagnetic Weiss temperature for $V_{1/3}NbS_2$ was reported to be negative, which is unexpected for a ferromagnetic material, and therefore was attributed to a large contribution from crystal field effects [11]. However, a more recent study on the magnetism of $V_{1/3}NbS_2$ and its sister compound $V_{1/3}TaS_2$ using neutron diffraction and dc susceptibility measurements reported that both of these materials are canted antiferromagnets, as expected for materials with negative Weiss temperatures [25]. This study also found evidence for a $\mathbf{k} = (0, 0, 0)$ magnetic propagation vector and described the magnetic structure of the material as an A-type antiferromagnet with some canting present along the c axis described by the coupling of two irreducible representations.

In this paper we present a detailed investigation into the magnetism of $V_{1/3}NbS_2$, using well-characterized single crystal and polycrystalline material. We have used techniques such as powder and single-crystal neutron diffraction, as well as heat capacity and magnetization measurements, to probe the magnetic structure of $V_{1/3}NbS_2$. We show that $V_{1/3}NbS_2$ becomes antiferromagnetic below 50 K. Two magnetic propagation vectors have been extracted from the powder neutron diffraction data: $\mathbf{k_0} = (0, 0, 0)$ and $\mathbf{k_1} = (0, 0, \frac{1}{3})$. The $\mathbf{k_0}$ propagation vector represents an in-plane component of the magnetism, with antiferromagnetically coupled ferromagnetic layers of vanadium atoms. The $\mathbf{k_1}$ propagation vector represents a canting out of the plane. In addition, we provide evidence for diffuse magnetic scattering in this material.

II. EXPERIMENTAL DETAILS

Single-crystal samples were prepared by chemical vapor transport using iodine as a transport agent. Using this method, crystals ranging in size from 1 to 6 mm along their longest lengths, with thicknesses ranging from 0.5 to 3 mm, were synthesized. The samples were characterized with powder and single-crystal x-ray diffraction and electron diffraction to confirm that the samples were in the correct phase, with the V atoms found to be occupying the 2c Wyckoff positions. A more detailed description of the different methods used to characterize the crystals of this family will be reported in [26]. A backscattering x-ray Photonic-Science Laue camera system was used to assess the quality of the single crystals.

A Quantum Design Magnetic Property Measurement System was used to measure the magnetization between 1.8 and 300 K in applied magnetic fields up to 70 kOe. Field-dependent magnetization measurements up to 100 kOe were performed using an Oxford Instruments vibrating sample magnetometer. The magnetic field was applied parallel and perpendicular to the c axis. The samples were aligned along the different crystallographic directions to within 1°–2°.

Heat capacity measurements were performed in a Quantum Design Physical Property Measurement System using the 2τ thermal relaxation method at temperatures from 1.8 to 300 K in zero applied field. Apiezon N grease was used to ensure good thermal contact between the sample and the sample stage.

Powder and single-crystal neutron diffraction measurements were performed using the WISH instrument at the ISIS neutron source [27]. The powder neutron diffraction data were taken at zero field for a range of temperatures between 1.5 and 60 K. The powdered $V_{1/3}NbS_2$ was mounted inside a vanadium canister. The single-crystal $V_{1/3}NbS_2$ was attached to an aluminum holder using aluminum tape, and the alignment was checked *in situ* and found to be accurate to within 1°–2°. The single-crystal neutron diffraction data were collected in both the $(hk0)$ and $(h0l)$ scattering planes at 1.5 K for a range of magnetic fields between 0 and 80 kOe. For the measurements in the $(hk0)$ scattering plane, the magnetic field was applied parallel to the c axis, while in the $(h0l)$ scattering plane, the magnetic field was applied along the [110] direction. A further temperature scan was performed in the $(h0l)$ scattering plane, from 1.5 to 52 K in zero field. The large number of position-sensitive detectors within WISH provide good resolution and also allowed for data to be taken several degrees outside of both of these scattering planes, i.e., the $(hk \pm \frac{1}{3})$ peaks were accessible. The single-crystal neutron diffraction data were treated using the single-crystal interface of MANTIDPLOT [28], and the powder neutron diffraction data were analyzed with the FULLPROF software suite [29].

III. RESULTS AND DISCUSSION

A. Magnetization

A Laue pattern from the single crystal used for the following experiments (Fig. 2) indicates that the crystal is of high quality. The magnetic behavior in single-crystal $V_{1/3}NbS_2$ was investigated by measuring the temperature dependence of the dc magnetic susceptibility $\chi_{dc}(T)$ in a field of 330 Oe applied either parallel or perpendicular to the c axis (Fig. 3). Fits to the zero-field-cooled (ZFC) data in the paramagnetic state using the Curie-Weiss law gave an effective moment of

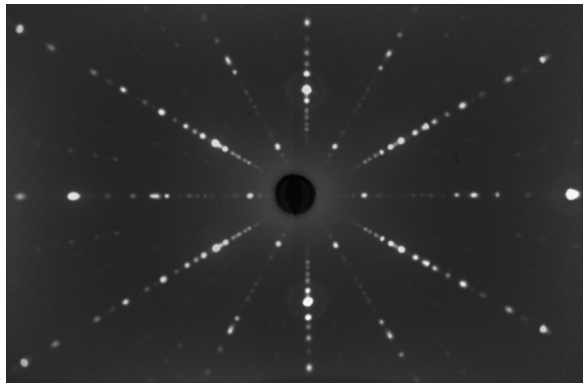

FIG. 2. Laue back-reflection pattern along the [001] orientation of an aligned $V_{1/3}NbS_2$ crystal.

$2.90(2)\mu_B$/f.u. and $3.03(2)$ μ_B/f.u. for the fields parallel and perpendicular to c, respectively. These values are both close to the expected spin-only value for V^{3+} of $2.83\mu_B$/f.u. and in agreement with previous work [11].

The material orders magnetically at 50 K. A larger signal is observed for $H \parallel c$; however, the moment measured is still far smaller than would be expected for a ferromagnetic material, despite the sharp increase in the susceptibility observed in the field-cooled-cooling (FCC) susceptibility. There is a significant difference between the ZFC and FCC curves for both field directions, and for $H \perp c$ an additional upturn in $\chi_{dc}(T)$ is observed at $T < 10$ K. The differences between these data and a recent study [25] can be explained due to the highly anisotropic nature of $V_{1/3}NbS_2$ and the fact that our measurements were carried out on single crystals of $V_{1/3}NbS_2$ as opposed to polycrystalline material.

The magnetization M as a function of magnetic field H is shown in Fig. 4. For all temperatures, when the field is applied

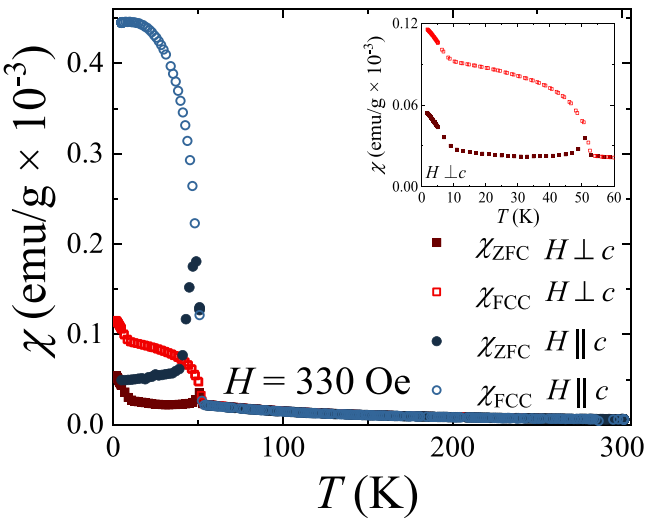

FIG. 3. Temperature dependence of the dc magnetic susceptibility χ_{dc} for $V_{1/3}NbS_2$ collected in ZFC and FCC modes in an applied field of $H = 330$ Oe for $H \parallel c$ and $H \perp c$. The inset shows the magnetic susceptibility for $H \perp c$ between 1.8 and 50 K, with a magnetic transition visible at 50 K.

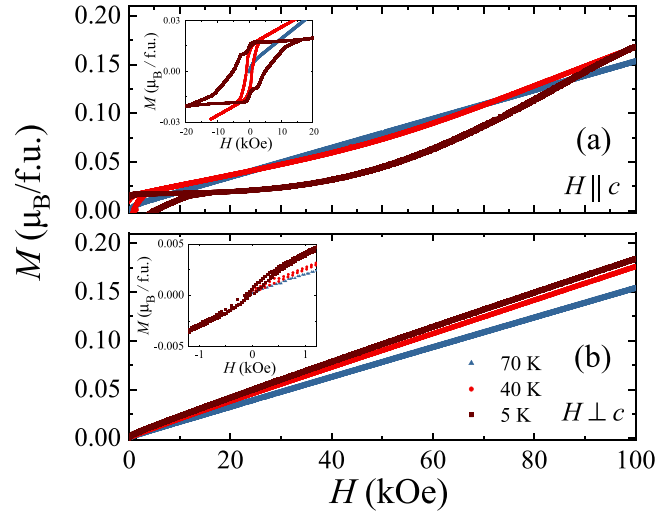

FIG. 4. Field dependence of the magnetization M per formula unit of VNb_3S_6 for various temperatures. The field was applied (a) parallel and (b) perpendicular to the c axis. The insets show the low-field hysteresis for both field directions.

perpendicular to c, a small amount of hysteresis is observed [Fig. 4(b), inset]. However, when the magnetic field is applied parallel to c, a significant hysteresis with a coercive field of up to 10 kOe is observed. Steplike features are also observed in the magnetic hysteresis loop at low fields when the magnetic field is applied at any, even very small, intermediate angle between exactly perpendicular and parallel to the c axis. The magnetization data indicate long-range magnetic order with a canting of the ordered magnetic moments.

The magnetization of $V_{1/3}NbS_2$ does not saturate in fields of up to 100 kOe regardless of the crystal orientation. As can be seen in Fig. 4, a maximum magnetization of $\approx 0.2\mu_B$/f.u. is reached by 100 kOe, which is significantly lower than the expected moment for V^{3+}. This large difference between the observed and expected moments, despite the full effective moment obtained from the Curie-Weiss fits in the paramagnetic state (Fig. 3), strongly indicates that the ordered magnetic structure is largely antiferromagnetic, with near-perfect cancellation of the moments between the magnetic sublattices, and that the introduction of a magnetic field does not significantly modify this structure.

B. Heat capacity

The heat capacity as a function of temperature for $V_{1/3}NbS_2$ is shown in Fig. 5. An anomaly at 50 K is clearly visible, indicating a magnetic transition. At low temperatures, $C(T)/T = \gamma + \beta T^2$ (Fig. 5, inset), where γ is the electronic contribution to the heat capacity and $\beta = \frac{12}{5}\frac{nR\pi^4}{\Theta_D^3}$, where $n = 10$ is the number of atoms per formula unit of VNb_3S_6, R is the molar gas constant, and Θ_D is the Debye temperature. A fit gives $\gamma = 7.5(2)$ mJ/mol K^2, a value that is reasonable for a metallic material [12]. Disorder in layered materials has been shown to increase γ [30,31]. Disorder of this kind is also prevalent in intercalated TMDCs and may also contribute to γ.

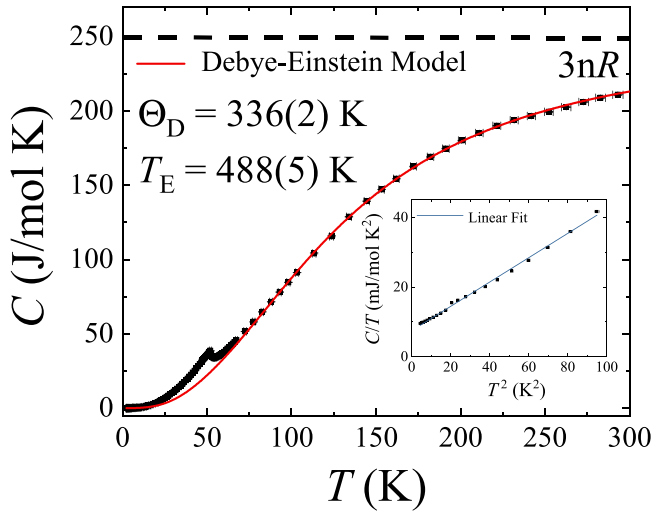

FIG. 5. Heat capacity C of $V_{1/3}NbS_2$ as a function of temperature T from 1.8 to 300 K. The line is a fit using the Debye-Einstein model. The inset shows the linear behavior of C/T as a function of T^2 at low temperatures, giving $\gamma = 7.5(2)$ mJ/mol K^2 and $\Theta_D = 382(2)$ K.

The Debye temperature $\Theta_D = 382(2)$ K, obtained from the fit, is consistent with the heat capacity at 300 K falling below the expected saturation value of $3nR$. A magnetic contribution to the heat capacity, assuming three-dimensional antiferromagnetic spin waves, would be proportional to T^3, making such a contribution difficult to distinguish from phonons, although the linear dependence of $C(T)/T$ vs T^2 is compatible with antiferromagnetic ordering. Such a contribution to C would result in a higher value for Θ_D, which is also consistent with the higher-temperature data.

In order to determine the entropy associated with the magnetic ordering, it is first necessary to remove the lattice contribution from the heat capacity. This phonon contribution can be estimated using a Debye-Einstein model:

$$C_{D-E}(T) = \gamma T + n\delta C_D\left(\frac{T}{\Theta_D}\right) + n(1-\delta)C_E\left(\frac{T}{T_E}\right), \quad (1)$$

where C_D is the Debye contribution, C_E is the Einstein contribution, δ is the fractional contribution of C_D, and T_E is the Einstein temperature. The heat capacity data were fitted using Eq. (1), as shown in Fig. 5. To limit the number of free parameters in this fit, γ was fixed to the value obtained from the low-temperature data. Of the $n = 10$ atoms present, the V and (three) Nb atoms are heavy compared to six lighter sulfur atoms. These heavier atoms can be well modeled with C_D, while the lighter sulfur atoms are modeled by the Einstein contribution C_E. We therefore constrain the fractional contribution δ to 0.4 to reflect this behavior. To ensure any magnetic contribution to the entropy is not accidentally removed when estimating the phonon contribution to the heat capacity, the Debye-Einstein fit was made from 80 to 300 K and then extrapolated to zero temperature. These considerations were helpful in confining the very flexible Debye-Einstein model to what is physically reasonable. A good fit to the data was obtained with a Debye temperature $\Theta_D = 336(2)$ K and an Einstein temperature $T_E = 488(5)$ K. These values seem reasonable as the expected Dulong-Petit value of $30R$ is not reached at 300 K and because they fall on either side of $\Theta_D = 382(2)$ K obtained from the low-temperature fit.

The change in entropy over the magnetic transition was calculated by integrating over $\Delta C/T$, where $\Delta C(T) = C(T) - C_{D-E}(T)$ and gave $\Delta S = 9(1)$ J/mol K, which is within error of the expected result of $\Delta S = R\ln 3$ from the $S = 1$ spin-only moment of V^{3+}. These data give strong evidence of long-range magnetic ordering in $V_{1/3}NbS_2$ with magnetic correlations above the ordering temperature.

C. Powder neutron diffraction

Powder neutron diffraction profiles for several different temperatures between 5 and 52 K are displayed in Fig. 6(a), with the data range restricted to between 3 and 5.5 Å to better show the evolution of two of the magnetic Bragg peaks. Any changes to the size and shape of the magnetic peaks at temperatures below 20 K are marginal. A significant decrease in peak intensity for the magnetic peaks occurs between 37.5 and 41 K, and the peaks continue to decrease further until their disappearance approaching the ordering temperature at 47 K.

The data taken at 5 K using the WISH banks with an average 2θ value of 54° are shown in Fig. 6(b) along with the calculated fit in the models for nuclear and magnetic structures, which is discussed below. A previous neutron diffraction study [25] reported a $\mathbf{k_0} = (0, 0, 0)$ propagation vector for the magnetic structure of both $V_{1/3}NbS_2$ and $V_{1/3}TaS_2$. Our data are consistent with the presence of the $\mathbf{k_0}$ magnetic reflections; however, there is another set of reflections which cannot be accounted for using just this propagation vector. Indexing of these reflections requires a second propagation vector $\mathbf{k_1} = (0, 0, \frac{1}{3})$. With the current data we cannot unambiguously confirm whether these two propagation vectors belong to the same or different phases. However, the fact that both the $\mathbf{k_0}$ and $\mathbf{k_1}$ reflections appear at the same temperature [Fig. 6(a)], within the accuracy of our measurements, indirectly suggests that they originate from the same magnetic phase.

The $\mathbf{k_0}$ magnetic intensities can be fitted with a model involving ferromagnetic layers, antiferromagnetically stacked along the c axis [Fig. 7(a)] [25]. The refined moment extracted from our data and associated with this model is $0.90(5)\mu_B$. The spins were found to be confined in the ab plane. It has been suggested that the structure might be canted with a small ferromagnetic component along the c axis [25]. The presence of this component is consistent with our magnetization data (Figs. 3 and 4); however, the origin of the coupling between the ferromagnetic and antiferromagnetic components requires particular consideration. The in-plane antiferromagnetic component is transformed by the two-dimensional irreducible representation $m\Gamma_5(\eta_1, \eta_2)$ of the $P6_322$ space group, while the out-of-plane ferromagnetic component is transformed by the $m\Gamma_2(\delta)$ representation (Table I) [32,33]. Thus, the antiferromagnetic and ferromagnetic order parameters have distinct symmetries and cannot be coupled via the bilinear free-energy invariant as in the typical case of a weak antiferromagnet [34]. The two components, however, are coupled via a linear-cubic term, $3\delta\eta_1^2\eta_2$-$\delta\eta_2^3$ [32]. The coupling is sensitive to the in-plane direction of the antiferromagnetic component and vanishes for the $(\eta_1, 0)$ order parameter, corresponding

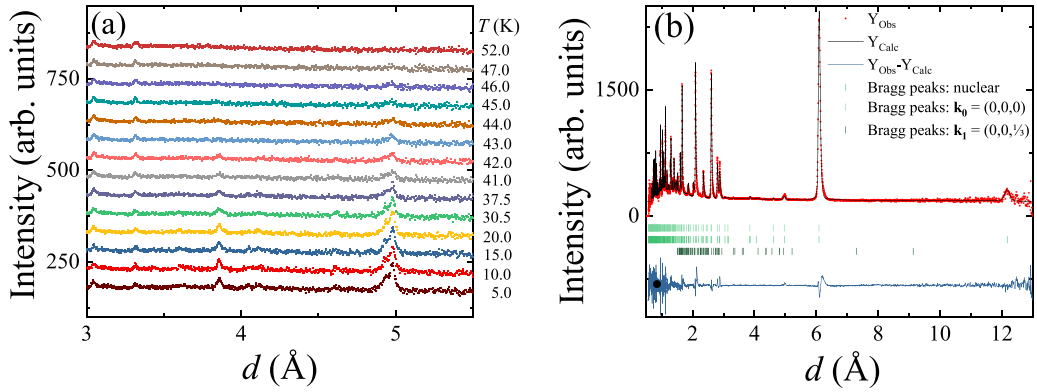

FIG. 6. (a) Evolution of the powder neutron diffraction profiles with temperatures for $V_{1/3}NbS_2$ between 5 and 52 K. For clarity, each profile is offset by 50 units. (b) Powder diffraction profile at 5 K with a calculated fit using a hexagonal, $P6_322$ structure and magnetic components with propagation vectors $\mathbf{k_0} = (0, 0, 0)$ and $\mathbf{k_1} = (0, 0, \frac{1}{3})$. The Bragg positions for each phase are shown below the pattern. The reliability factors are $R_{\text{Bragg}} = 6.1$ for the atomic structure and $R_{\text{Mag}} = 19.2$ and 30.9 for the magnetic structures with the $\mathbf{k_0}$ and $\mathbf{k_1}$ propagation vectors, respectively.

to the magnetic space group $C222_1$ [33] and the case when the V spins are perpendicular to the a axis. The coupling is allowed and is maximal for another high symmetry order parameter direction, $(0, \eta_2)$, corresponding to the magnetic space group $C2'2'2_1$ and the V spins parallel to the a axis. Thus, based on the magnetization data (Figs. 3 and 4) and the symmetry arguments, one can conclude that the $\mathbf{k_0}$ antiferromagnetic component in $V_{1/3}NbS_2$ is likely to be along the a axis. A similar coupling between in-plane antiferromagnetic and out-of-plane ferromagnetic components through the linear-cubic free-energy term was recently discussed for the trigonal ruthenates Sr_3ARuO_6, with $A = (\text{Li}, \text{Na})$ [35]. It was concluded that the microscopic interaction behind this coupling is the magnetoelastically induced antisymmetric Dzyaloshinskii-Moriya exchange. The magnetoelastic coupling is anisotropic, and it depends on the in-plane direction of the spins. This breaks the degeneracy between the different in-plane antiferromagnetic configurations choosing a particular direction, which activates the additional antisymmetric energy term.

We now discuss the $\mathbf{k_1}$ component. The crucial observation is the absence of $(0, 0, l) \pm \mathbf{k_1}$ magnetic satellites, which strongly indicates that this spin component is along the c axis. The symmetry analysis based on representation theory [33] reveals two two-dimensional irreducible representations associated with $\mathbf{k_1}$ and transforming the out-of-plane spin component, $m\Delta_1(\rho_1, \rho_2)$ and $m\Delta_2(\xi_1, \xi_2)$ (Table I). Both describe longitudinal spin density waves whose global magnetic phase is controlled by the order parameter direction

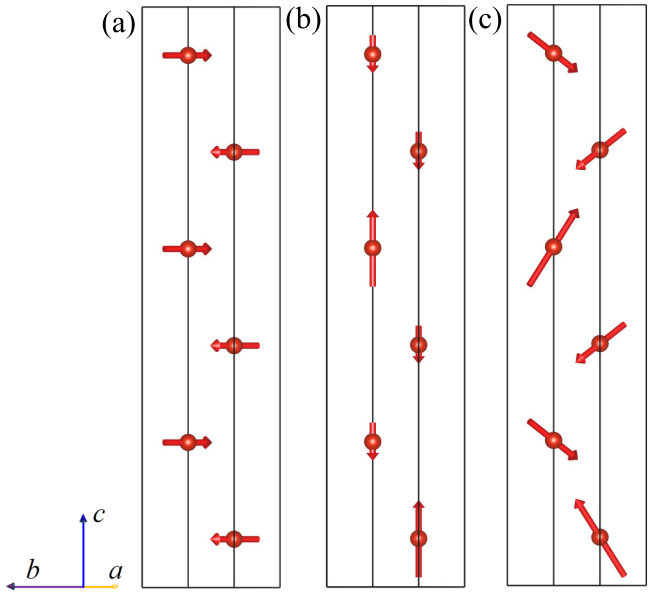

FIG. 7. Magnetic moments on the vanadium atoms in a unit cell of $V_{1/3}NbS_2$ viewed along the a^* direction. (a) In-plane moments associated with the $\mathbf{k_0} = (0, 0, 0)$ propagation vector, (b) the out-of-plane up-down-down moments associated with the $\mathbf{k_1} = (0, 0, \frac{1}{3})$ propagation vector, and (c) the superposition of these two components.

TABLE I. Atomic components of the basis functions localized on the 2c Wyckoff position of the $P6_322$ paramagnetic space group and transformed by the irreducible representations (irrep) associated with $\mathbf{k_0} = (0, 0, 0)$ ($m\Gamma_2$ and $m\Gamma_5$) and $\mathbf{k_1} = (0, 0, \frac{1}{3})$ ($m\Delta_1$ and $m\Delta_2$) propagation vectors.

Irrep	$V_1\left(\frac{1}{3}, \frac{2}{3}, \frac{1}{4}\right)$	$V_2\left(\frac{2}{3}, \frac{1}{3}, \frac{3}{4}\right)$
$m\Gamma_5$		
η_1	$\left(\frac{1}{3}, \frac{2}{\sqrt{3}}, 0\right)$	$\left(-\frac{1}{2}, -\frac{2}{\sqrt{3}}, 0\right)$
η_2	$(1, 0, 0)$	$(-1, 0, 0)$
$m\Gamma_2$		
δ	(0,0,1)	(0,0,1)
$m\Delta_1$		
ρ_1	$\left(0, 0, \frac{1}{2}\right) + i\left(0, 0, -\frac{\sqrt{3}}{2}\right)$	$(0, 0, 1) + i(0, 0, 0)$
ρ_2	$\left(0, 0, \frac{\sqrt{3}}{2}\right) + i\left(0, 0, \frac{1}{2}\right)$	$(0, 0, 0) + i(0, 0, 1)$
$m\Delta_2$		
ξ_1	$\left(0, 0, \frac{\sqrt{3}}{2}\right) + i\left(0, 0, \frac{1}{2}\right)$	$(0, 0, 0) + i(0, 0, -1)$
ξ_2	$\left(0, 0, -\frac{1}{2}\right) + i\left(0, 0, \frac{\sqrt{3}}{2}\right)$	$(0, 0, 1) + i(0, 0, 0)$

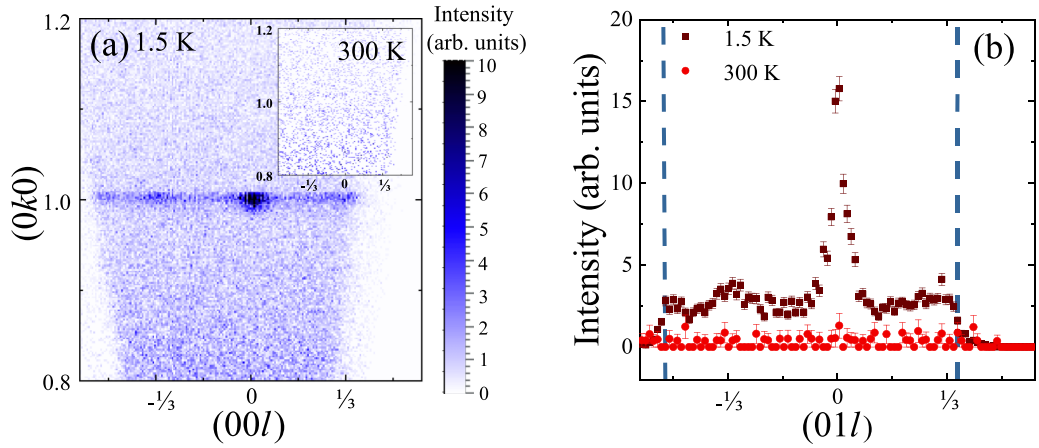

FIG. 8. (a) Area detector image depicting the (010) and (01$\pm\frac{1}{3}$) Bragg peaks and the diffuse scattering between them, with $H \parallel c$. (b) Cut taken from the area detector image along [01l] at 1.5 and 300 K to compare the intensities of the peaks with the intensity of the diffuse scattering. The limits of the detector are shown as dashed blue lines.

(admixing coefficients ρ_1/ρ_2 and ξ_1/ξ_2). The difference between $m\Delta_1$ and $m\Delta_2$ is the relative magnetic phase between the spin density waves localized on the two V sites. In the former case the difference is $\frac{\pi}{3}$, and in the latter case it is $\frac{2\pi}{3}$.

The quantitative refinement of the neutron diffraction data indicates that the $m\Delta_2$ representation provides a better fitting quality [Fig. 6(b)]. It is well known that neutron diffraction is not sensitive to the global magnetic phase, and therefore, we cannot experimentally determine the order parameter direction in the $m\Delta_2$ representation space. The magnetic symmetry (magnetic space group), however, depends on the global phase, and this fact can provide additional information through various coupling phenomena controlled by the symmetry. In particular, a coupling of the macroscopic ferromagnetic component along the c axis is possible when the order parameter takes the $(0, \xi_2)$ direction in the representation space. The relevant coupling term is similar to the one discussed above, $3\delta\xi_1^2\xi_2$-$\delta\xi_2^3$. The corresponding magnetic structure is the up-down-down type with the $P6_32'2'$ magnetic space group [Fig. 7(b)]. The two moment values were refined as $1.21(12)\mu_B$ (up) and $0.61(6)\mu_B$ (down). The up and down spin components are not constrained by the symmetry to compensate one other, resulting in a net ferrimagnetic moment, which is, however, too small to be refined from the neutron diffraction data. Thus, the experimentally observed weak ferromagnetism (Figs. 3 and 4) can also be explained by the small ferrimagnetic moment associated with the $\mathbf{k_1}$ component. It is possible that coupling between the in-plane $\mathbf{k_0}$ and out-of-plane $\mathbf{k_1}$ magnetic order parameters takes place via the common ferromagnetic component shared by these order parameters in the scenario where both $\mathbf{k_0}$ and $\mathbf{k_1}$ belong to the same magnetic phase. In the latter case, the resultant magnetic space group which accounts for the presence of both propagation vectors [Fig. 7(c)] is $C2'2'2_1$, with the lattice vectors and origin related to the parent $P6_322$ paramagnetic space group as (0,1,0), $(-2, -1, 0)$, (0,0,3), and (0,0,0) [33]. In this case, each moment is canted significantly out of plane, with the "down" vectors experiencing a cant of 34° out of plane and the "up" vectors being canted 55° out of plane in the opposite direction.

Finally, let us note that the antisymmetrized square of both $m\Gamma_5$ and $m\Delta_2$ irreducible representations contains the vector representation. This implies that Lifshitz invariants [36] promoting inhomogeneous long-period modulated states are allowed in the free-energy decomposition. In particular, these types of invariants are responsible for the formation of the magnetic helical state [37] and the field-induced chiral soliton lattice in $Cr_{1/3}NbS_2$ [38] as well as in some other systems with noncentrosymmetric crystal structures, such as MnSi [39], $Ca_3Ru_2O_7$ [40], and $BiFeO_3$ [41]. It is not clear why the commensurate ground state in $V_{1/3}NbS_2$ is robust against the chiral interactions behind the Lifshitz terms. A possible explanation is that the magnetoelastic coupling and associated anisotropic interactions discussed above are stronger and dominate in this compound.

D. Single-crystal neutron diffraction

Extracting the magnetic structure from powder neutron diffraction measurements alone can be challenging. Single-crystal neutron diffraction measurements were performed to confirm the suitability of the possible magnetic structures obtained from powder neutron diffraction.

The (010) peak was initially examined in the configuration for the (hk0) scattering plane. The magnetic field was applied parallel to the c axis, and the large out-of-plane coverage of the WISH detectors allowed us to take data several degrees outside of this scattering plane along l. An example of the zero-field intensity maps at 1.5 and 300 K is given in Fig. 8. For clarity, in Fig. 8(b), a cut taken along [01l] with a width of 0.1 in h is presented.

Peaks exist at (01$\frac{1}{3}$) and (01$-\frac{1}{3}$) that can be associated with the $\mathbf{k_1}$ magnetic propagation vector. Diffuse scattering is clearly visible between the (010) peak and the (01 $\pm\frac{1}{3}$) peaks flanking it, and this scattering appears to be magnetic in nature, as it disappears above the transition temperature 50 K (see 300 K data in the inset). In Fig. 8(b) the line plot of the (010) and (01$\pm\frac{1}{3}$) peaks is displayed, showing that the latter two peaks exist above the diffuse scattering. These data were taken as a slice at (10l). This diffuse scattering implies

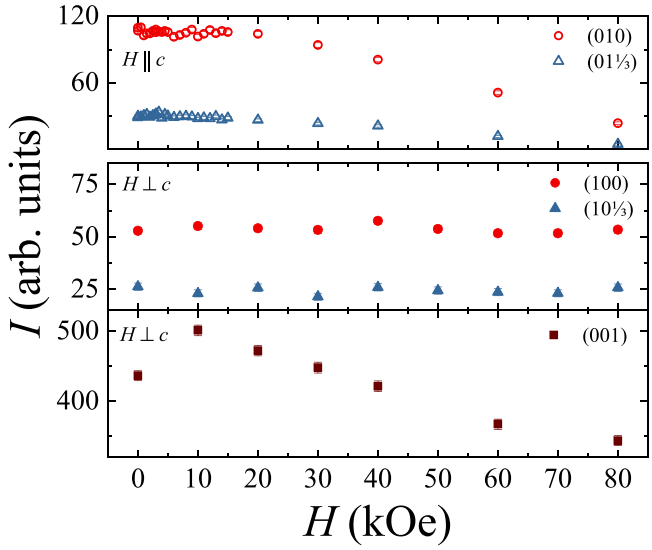

FIG. 9. Integrated intensity I of several different structural and magnetic peaks and their dependence on applied magnetic field. Field dependence of the integrated intensities of the (010) and $(01\frac{1}{3})$ peaks with the field directed $H \parallel c$ (top). Integrated intensities of the (100) and $(10\frac{1}{3})$ peaks (middle) and (001) peaks (bottom) in the $(h0l)$ scattering plane with the field directed along [110].

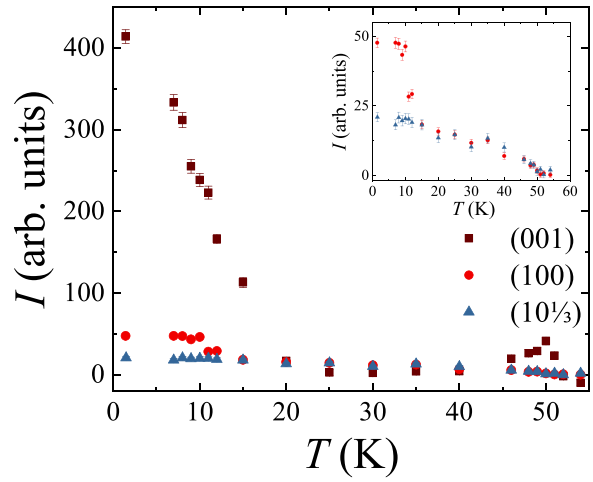

FIG. 10. Integrated intensity I of several different structural and magnetic peaks and their dependence on temperature. The integrated intensities of the (100), $(10\frac{1}{3})$ and (001) peaks between 1.5 and 54 K are plotted on the same axes. The inset depicts the region of interest for the (100) and $(10\frac{1}{3})$ peaks.

the presence of a level of disorder to the magnetic structure and appears between peaks that correspond to the $\mathbf{k_0}$ and $\mathbf{k_1}$ propagation vectors.

Figure 9 shows the integrated intensities of the peaks of interest for several different applied field strengths. The (001) peak was examined and shows an increase in intensity upon the application of a magnetic field up to 10 kOe in strength, before steadily decreasing between 10 and 80 kOe in a manner consistent with antiferromagnetism. The magnetism of this peak can be associated with the magnetic propagation vector $\mathbf{k_0}$ and does not show the same behavior as the (100) and associated peaks.

The (100) peak in the $(h0l)$ scattering plane shows behavior similar to the (010) peak in the $(hk0)$ scattering plane at zero field; that is, diffuse scattering exists that is no longer present above the magnetic transition temperature. However, a magnetic field scan reveals that the two peaks evolve differently under the influence of an external magnetic field (see Fig. 4). The (010) and $(01\pm\frac{1}{3})$ peaks, under a magnetic field applied parallel to the c axis, begin to decrease in intensity as the magnetic field increases between 20 and 80 kOe. The (100) and $(10\pm\frac{1}{3})$ peaks, however, do not change significantly in intensity for an applied field along the [110] direction between 0 and 80 kOe. This must be related to the direction of the applied field as these two peaks are equivalent for a hexagonal system.

Figure 10 displays the temperature dependence of the integrated intensities of certain Bragg peaks in the $(h0l)$ scattering plane. While the $(10\pm\frac{1}{3})$ peaks show a steady decrease in intensity as the temperature increases, the (100) and (001) peaks show a sharper decrease in intensity between 10 and 20 K, which coincides with the additional transition visible in the dc susceptibility data in Fig. 3. It is worth noting that the (100) and $(10\frac{1}{3})$ peaks sit on a background of diffuse scattering that was not present around the (001) peak.

The (001) peak intensity at temperatures below 20 K is far greater than the corresponding intensities of the (100) and $(10\frac{1}{3})$ peaks. It then drops to approximately zero between 20 and 50 K, which is considerably lower than the corresponding (100) and $(10\frac{1}{3})$ peak intensities, before briefly increasing in intensity at the ordering temperature. The behavior of the (001) peak is remarkably reminiscent of the behavior seen in dc susceptibility data for H applied perpendicular to the c axis in Fig. 3.

IV. SUMMARY

In summary, the magnetic structure of $V_{1/3}NbS_2$ has been investigated using dc susceptibility, heat capacity, and powder and single-crystal neutron diffraction measurements. $V_{1/3}NbS_2$ was found to undergo a magnetic transition at $T_N = 50$ K. The powder neutron diffraction data revealed the presence of two magnetic propagation vectors, $\mathbf{k_0} = (0, 0, 0)$ and $\mathbf{k_1} = (0, 0, \frac{1}{3})$, which could be fit to magnetic structures with antiferromagnetic stacking of vanadium layers and a canting along the c axis, respectively. This explains the lack of saturation that is observed in the magnetization even in magnetic fields of 100 kOe, as well as the sharp increase of the dc susceptibility at 50 K in the FCC measurements. The presence of the $\mathbf{k_1}$ propagation vector opens the possibility of the expected ferromagnetic canting along the c axis originating from this propagation vector rather than from the $\mathbf{k_0}$ propagation vector as proposed earlier [25].

Analysis of the single-crystal neutron diffraction data revealed diffuse magnetic scattering between the (010) and $(01\pm\frac{1}{3})$ Bragg peaks, indicating a level of disorder in the magnetic structure of $V_{1/3}NbS_2$. Additionally, the magnetic structure seemed to be highly anisotropic, with the integrated intensity of the Bragg peaks dependent on the direction of the applied magnetic field, remaining constant in intensity

between 0 and 80 kOe for H in the ab plane and decreasing in intensity with increasing field for H parallel to the c axis.

Our study here, adopting a multitechnique approach, has shown that the material $V_{1/3}NbS_2$ has a complex magnetic structure that is very different from the magnetism previously observed in other members of this family such as $Mn_{1/3}NbS_2$ and the CSL observed in $Cr_{1/3}NbS_2$. Due to the nature of the canted antiferromagnetic ordering in this material, it seems unlikely that a CSL phase can be induced. In showing the existence of a secondary, mostly diffuse, component of the magnetic structure associated with the $\mathbf{k_1}$ propagation vector, we have uncovered greater detail about the magnetic structure of this material.

ACKNOWLEDGMENTS

This work was financially supported by the Engineering and Physical Sciences Research Council (EPSRC) (Grant No. EP/N032128/1). This work was supported by UKRI and Science and Technology Facilities Council (STFC) through the provision of beam time at the ISIS Neutron and Muon Source [42].

[1] R. Yan, G. Khalsa, B. T. Schaefer, A. Jarjour, S. Rouvimov, K. C. Nowack, H. G. Xing, and D. Jenal, Appl. Phys. Express **12**, 023008 (2019).
[2] A. H. Castro Neto, Phys. Rev. Lett. **86**, 4382 (2001).
[3] R. L. Withers and J. A. Wilson, J. Phys. C **19**, 4809 (1986).
[4] J. A. Wilson, F. J. Di Salvo, and S. Mahajan, Adv. Phys. **24**, 117 (1975).
[5] K. Rossnagel, J. Phys.: Condens. Matter **23**, 213001 (2011).
[6] Z. Zhang, X. Zou, V. H. Crespi, and B. I. Yakobson, ACS Nano **7**, 10475 (2013).
[7] Z. Guguchia *et al.*, Sci. Adv. **4**, eaat3672 (2018).
[8] S. Tang, R. S. Fishman, S. Okamoto, J. Yi, Q. Zou, M. Fu, A.-P. Li, D. Mandrus, and Z. Gai, Nano. Lett. **18**, 4023 (2018).
[9] J. Lee, S. Pak, Y.-W. Lee, Y. Park, A.-R. Jang, J. Hong, Y. Cho, B. Hou, S. Lee, H. Y. Jeong, H. S. Shin, S. M. Morris, S. Cha, J. I. Sohn, and J. M. Kim, ACS Nano **13**, 13047 (2019).
[10] J. M. van den Berg and P. Cossee, Inorg. Chim. Acta **2**, 143 (1968).
[11] S. S. P. Parkin and R. H. Friend, Philos. Mag. B **41**, 65 (1980).
[12] S. S. P. Parkin and R. H. Friend, Philos. Mag. B **41**, 95 (1980).
[13] S. S. P. Parkin and A. R. Beal, Philos. Mag. B **42**, 627 (1980).
[14] Y. Kousaka, Y. Nakao, J. Kishine, M. Akita, K. Inoue, and J. Akimitsu, Nucl. Instrum. Methods Phys. Res., Sect. A **600**, 250 (2009).
[15] Y. Kousaka, T. Ogura, J. Zhang, P. Miao, S. Lee, S. Torii, T. Kamiyama, J. Campo, K. Inoue, and J. Akimitsu, J. Phys.: Conf. Ser. **746**, 012061 (2016).
[16] A. Bauer and C. Pfleiderer, in *Topological Structures in Ferroic Materials: Domain Walls, Vortices and Skyrmions*, edited by J. Seidel (Springer International Publishing, Cham, 2016), pp. 1–28.
[17] S. Seki and M. Mochizuki, *Skyrmions in Magnetic Materials* (Springer, New York, 2016).
[18] Y. Togawa, T. Koyama, K. Takayanagi, S. Mori, Y. Kousaka, J. Akimitsu, S. Nishihara, K. Inoue, A. S. Ovchinnikov, and J. Kishine, Phys. Rev. Lett. **108**, 107202 (2012).
[19] G. W. Paterson, T. Koyama, M. Shinozaki, Y. Masaki, F. J. T. Goncalves, Y. Shimamoto, T. Sogo, M. Nord, Y. Kousaka, Y. Kato, S. McVitie, and Y. Togawa, Phys. Rev. B **99**, 224429 (2019).
[20] B. Van Laar, H. M. Rietveld, and D. J. W. Ijido, J. Solid State Chem. **3**, 154 (1971).
[21] N. L. Nair, E. Maniv, C. John, S. Doyle, J. Orenstein, and J. G. Analytis, Nat. Mater. **19**, 153 (2020).
[22] A. Little, C. Lee, C. John, S. Doyle, E. Maniv, N. L. Nair, W. Chen, D. Rees, J. W. F. Venderbos, R. M. Fernandes, J. G. Analytis, and J. Orenstein, Nat. Mater. **19**, 1062 (2020).
[23] F. Hulliger and E. Pobitschka, J. Solid State Chem. **1**, 117 (1970).
[24] L. M. Volkova and D. V. Marinin, J. Appl. Phys. **116**, 133901 (2014).
[25] K. Lu, D. Sapkota, L. DeBeer-Schmitt, Y. Wu, H. B. Cao, N. Mannella, D. Mandrus, A. A. Aczel, and G. J. MacDougall, Phys. Rev. Mater. **4**, 054416 (2020).
[26] A. E. Hall, J. C. Loudon, P. Midgley, A. C. Twitchett-Harrison, S. J. R. Holt, D. A. Mayoh, Y. Han, M. R. Lees, and G. Balakrishnan (unpublished).
[27] L. C. Chapon, P. Manuel, P. G. Radaelli, C. Benson, L. Perrott, S. Ansell, N. J. Rhodes, D. Raspino, D. Duxbury, E. Spill, and J. Norris, Neutron News **22**, 22 (2011).
[28] O. Arnold *et al.*, Nucl. Instrum. Methods Phys. Res., Sect. A **764**, 156 (2014).
[29] J. Rodríguez-Carvajal, Physica B **192**, 55 (1993).
[30] P. M. Ostrovsky, V. Gornyi, and A. D. Mirlin, Phys. Rev. B **74**, 235443 (2006).
[31] I. Grosu and T.-L. Biter, Phys. Lett. A **382**, 3042 (2018).
[32] H. T. Stokes, D. M. Hatch, and B. J. Campbell, ISOTROPY software suite, https://iso.byu.edu/iso/isotropy.php.
[33] B. J. Campbell, H. T. Stokes, D. E. Tanner, and D. M. Hatch, J. Appl. Crystallogr. **39**, 607 (2006).
[34] I. Dzyaloshinsky, J. Phys. Chem. Solids **4**, 241 (1958).
[35] D. G. Porter, M. S. Senn, D. D. Khalyavin, A. Cortese, N. Waterfield-Price, P. G. Radaelli, P. Manuel, H.-C. zur-Loye, C. Mazzoli, and A. Bombardi, Phys. Rev. B **94**, 134404 (2016).
[36] L. D. Landau and E. M. Lifshitz, *Statistical Physics, Course of Theoretical Physics*, 3rd ed., Vol. 5 (Pergamon Press, Oxford, 1997).
[37] T. Moriya and T. Miyadai, Solid State Commun. **42**, 209 (1982).
[38] Y. Togawa, Y. Kousaka, K. Inoue, and J.-I. Kishine, J. Phys. Soc. Jpn. **85**, 112001 (2016).
[39] S. Mühlbauer, B. Binz, F. Jonietz, C. Pfleiderer, A. Rosch, A. Neubauer, R. Georgii, and P. Böni, Science **323**, 915 (2009).
[40] C. D. Dashwood, L. S. I. Veiga, Q. Faure, J. G. Vale, D. G. Porter, S. P. Collins, P. Manuel, D. D. Khalyavin, F. Orlandi,

R. S. Perry, R. D. Johnson, and D. F. McMorrow, Phys. Rev. B **102**, 180410(R) (2020).

[41] A. M. Kadomtseva, A. K. Zvezdin, Y. F. Popov, A. P. Pyatakov, and G. P. Vorob'ev, JETP Lett. **79**, 571 (2004).

[42] G. Balakrishnan, M. R. Lees, D. A. Mayoh, P. Manuel, A. E. Hall, and O. A. Petrenko, A neutron diffraction study of $V_{1/3}NbS_2$: determination of the magnetic ground state and the effects of magnetic field (STFC ISIS Neutron and Muon Source, 2020), doi:10.5286/ISIS.E.RB2010556-1.